ISBI'08, IEEE International Symposium on BioImaging, April 2008. (Preprint)

BREAST CANCER DETECTION BY TIME REVERSAL IMAGING

*Yuanwei Jin, José M.F. Moura, and Yi Jiang**

Electrical and Computer Engineering
Carnegie Mellon University
Pittsburgh, PA 15213
{ywjin, moura, yij}ece.cmu.edu

Michael Wahl, He Zhu, and Qiuhong He†

University of Pittsburgh
University of Pittsburgh Medical Center
Pittsburgh, PA 15213
{mww3+,hezst2+}@pitt.edu, heq@upmc.edu

ABSTRACT

This paper examines a time reversal beamforming imager for detecting early stage breast cancer tumors. We use numerical simulations and electromagnetic tissue experiments to validate the imager. Microwave radiation is known to be a potential diagnostic imaging tool for breast cancer detection that could complement the standard X-ray mammography. Electromagnetic radiation waves undergo multiple scattering due to the inhomogeneities of biological tissues. In this paper, we demonstrate that our proposed time reversal imager exploits successfully the multiple path electromagnetic scattering to achieve higher resolution and robustness than the direct subtraction beamforming imager.

***Index Terms*—** Time reversal, Electromagnetic radiation, Breast cancer detection, Beamforming

1. INTRODUCTION

Microwave imaging utilizes non-ionizing electromagnetic radiation to detect cancer tumors in a human body. Over the years, research has shown that microwave breast cancer detection may become a successful clinical complement to conventional X-ray mammography [1, 2, 3]. In microwave imaging, several microwave emitters illuminate the breast. The resulting scattered field is measured at multiple detectors. Malignant breast tumors have electrical properties that are significantly different from those of healthy breast tissues [4, 5, 6]. The cancerous tumors produce stronger backscattered EM energy return than normal tissues. In principle, it is then possible to locate the tumors and reconstruct their shapes. However, unlike X-rays, which are non-diffractive and travel in straight lines, EM microwave propagation in breast tissues is characterized by refraction and multipath effects, i.e., the backscattered cancer signature signal reaches the detector by two or more paths. As a result, standard data processing algorithms do not perform well due to the multipath propagation and cannot identify and locate cancer tumors with high accuracy and fine resolution.

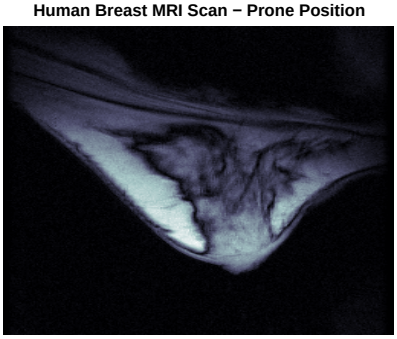

Fig. 1. MRI scan of a human breast in the prone position

Time reversal can make use of scattering to achieve high resolution. This motivated research to apply time reversal to medical imaging, e.g., in ultrasound [7] and EM [3, 8]. **Our hypothesis** is that time reversal based beamforming imaging exploits successfully the multiple path EM wave scattering due to the inhomogeneous breast tissues to detect and diagnose small cancer tumors with high sensitivity and high specificity. We validiated this hypothesis in [3] by numerical finite difference time domain (FDTD) modeling. This paper reports on our continuing work by showing the results we have obtained with (1) an anatomically realistic FDTD simulation model based on an MRI scan of a human breast; and (2) experimental electromagnetic data using animal tissues. Both cases demonstrate that time reversal enhances tumor detection and achieves high resolution.

2. TIME REVERSAL BEAMFORMING IMAGING

We describe the time reversal beamforming imager proposed in [3, 9]. The imager consists of two linear antenna arrays, A and B, in a multi-static configuration (see Fig. 2). We describe the imaging algorithms in the (discrete) frequency domain because time reversal in the time domain is equivalent to phase conjugation in the frequency domain. We transmit probe signals $S(\omega_q)$, $q = 1, \cdots, Q$, from array A; the waves reflect from the target (tumor) and arrive at the received ar-

*This joint work is funded by the Defence Advanced Research Projects Agency through the Army Research Office under grant no. W911NF-04-1-0031 and the Pennsylvania Infrastructure Technology Alliance through the Summer Undergraduate Research Experience program.

†This joint work is funded by the Susan G. Komen Breast Cancer Foundation under grant no. IMG0100117 and the National Institutes of Health under grant no. R01 CA109471-01 A1.

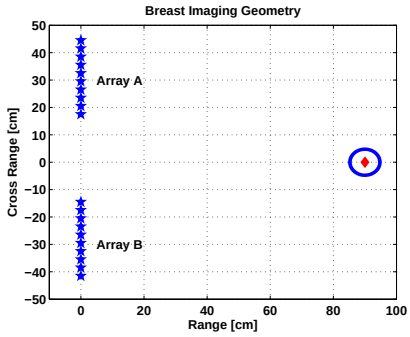

Fig. 2. Experiment Imaging Geometry

ray B. In time reversal, the received signals at array B are phase conjugated and retransmitted back to the medium. The frequency domain measured data are processed to detect the target (tumor) location. We carry out time reversal mathematically without physically re-transmitting the signals. Let $G(\mathbf{r}, \mathbf{r}'; \omega_q)$ denote the Green's function between transmitter $\mathbf{r}'$ and receiver $\mathbf{r}$ at frequency ω_q. For a reciprocal channel, the Green's function satisfies $G(\mathbf{r}, \mathbf{r}'; \omega_q) = G(\mathbf{r}', \mathbf{r}; \omega_q)$. The target response $\mathbf{K}_t(\omega_q)$ is

$$[\mathbf{K}_t(\omega_q)]_{ij} = G(\mathbf{r}_{B_i}, \mathbf{x}_t; \omega_q)\tau(\mathbf{x}_t)G(\mathbf{x}_t, \mathbf{r}_{A_j}; \omega_q), \quad (1)$$

where $\mathbf{x}_t$, $\mathbf{r}_{B_i}$, and $\mathbf{r}_{A_j}$ denote the locations of the target, the i-th and the j-th antennas of array B and array A. The symbol $\tau(\mathbf{x}_t)$ is the target reflectivity at location $\mathbf{x}_t$. In this paper, we work with the following Green's function:

$$G(\mathbf{r}, \mathbf{r}'; \omega_q) = \frac{1}{4j} H_0^{(2)}(k_q|\mathbf{r} - \mathbf{r}'|), \quad (2)$$

where $H_0^{(2)}$ is the zeroth-order Hankel function of the second kind; $k_q = \omega_q/v$ is the wavenumber of a propagating wave with angular frequency ω_q; and v is the medium propagation velocity. For a medium with relative permittivity ϵ_r and relative permeability μ_r, $v = \frac{1}{\sqrt{\epsilon_r \mu_r}} c$, c is the speed of light. We take that $\mu_r = 1$, thus $v = \frac{1}{\sqrt{\epsilon_r}} c$. Eqn. (2) yields the following Green's function vectors for arrays A and B:

$$\mathbf{g}_B(\mathbf{x}_t; \omega_q) = \left[G(\mathbf{r}_{B_0}, \mathbf{x}_t; \omega_q), \cdots, G(\mathbf{r}_{B_{N-1}}, \mathbf{x}_t; \omega_q)\right]^T$$
$$\mathbf{g}_A(\mathbf{x}_t; \omega_q) = \left[G(\mathbf{x}_t, \mathbf{r}_{A_0}; \omega_q), \cdots, G(\mathbf{x}_t, \mathbf{r}_{A_{P-1}}; \omega_q)\right]^T.$$

Our time reversal scheme has five steps [3, 9]:

Step-1: Clutter probing This is the training step and that no target is present. In our experiment, we assume that we obtain the *exact* clutter measurement. In reality, one can use time-domain gating to obtain the estimate of the strong reflections due to the skin layer across the frequency range of interest. It is also possible to utilize patients' chronicle EM screening data or to derive from other imaging modalities to estimate the clutter response matrix $\mathbf{K}_c(\omega_q)$ in this step.

Step-2: Time reversal clutter suppression In this step, we design an adaptive filter suppresses the clutter return by minimizing the total clutter returns [9]:

$$\mathbf{W}(\omega_q) = k_q \left[\mathbf{K}_c^*(\omega_q)\mathbf{K}_c^T(\omega_q)\right]^\dagger, \quad (3)$$

where $\dagger$ is the pseudo-inverse, and k_q is a scaling factor. Filtering with (3) whitens the clutter, which is subtracted out.

Step-3: Target monitoring This step probes the environment when the target can presumably be present. We apply the filter (3) to the received backscatter signals to suppress and subtract out the clutter.

Step-4: Time reversal target focusing The residual target signal is time reversed (or phase conjugated in frequency domain.) This leads to the clutter suppressed and target focused data matrices measured at array A and array B:

$$\mathbf{M}^B(\omega_q) = k_q \mathbf{K}_t(\omega_q) \mathbf{K}_t^H(\omega_q) \mathbf{K}_c^{-H}(\omega_q) S(\omega_q) \quad (4)$$
$$\mathbf{M}^A(\omega_q) = k_q \mathbf{K}_t^T(\omega_q) \mathbf{K}_t^*(\omega_q) \mathbf{K}_c^{-*}(\omega_q) S(\omega_q). \quad (5)$$

Step 5: Image formation. This step scans the area of interest with two focused beams by triangulation to extract target locations. Let $\mathbf{w}_{rB}(\mathbf{x}; \omega_q)$, $\mathbf{w}_{tB}(\mathbf{x}; \omega_q)$, $\mathbf{w}_{rA}(\mathbf{x}; \omega_q)$, and $\mathbf{w}_{tA}(\mathbf{x}; \omega_q)$ be the receive and transmit beams for arrays B and A, respectively, at frequency $\omega_q, \forall q$:

$$\mathbf{w}_{rB}(\mathbf{x}; \omega_q) = \frac{\mathbf{g}_B(\mathbf{x}; \omega_q)}{\|\mathbf{g}_B(\mathbf{x}; \omega_q)\|}, \quad (6)$$
$$\mathbf{w}_{tB}(\mathbf{x}; \omega_q) = \frac{\mathbf{K}_c^{-1}(\omega_q)\mathbf{g}_B(\mathbf{x}; \omega_q)}{\|\mathbf{K}_c^{-1}(\omega_q)\mathbf{g}_B(\mathbf{x}; \omega_q)\|}, \quad (7)$$
$$\mathbf{w}_{rA}(\mathbf{x}; \omega_q) = \frac{\mathbf{g}_A(\mathbf{x}; \omega_q)}{\|\mathbf{g}_A(\mathbf{x}; \omega_q)\|}, \quad (8)$$
$$\mathbf{w}_{tA}(\mathbf{x}; \omega_q) = \frac{\mathbf{K}_c^{-T}(\omega_q)\mathbf{g}_A(\mathbf{x}; \omega_q)}{\|\mathbf{K}_c^{-T}(\omega_q)\mathbf{g}_A(\mathbf{x}; \omega_q)\|}. \quad (9)$$

Applying the weight vectors to $\mathbf{M}^B(\omega_q)$ and $\mathbf{M}^A(\omega_q)$ lead to the outputs of the beamformers B and A

$$Y^B(\mathbf{x}; \omega_q) = \mathbf{w}_{rB}^H(\mathbf{x}; \omega_q) \mathbf{M}^B(\omega_q) \mathbf{w}_{tB}(\mathbf{x}; \omega_q), \quad (10)$$
$$Y^A(\mathbf{x}; \omega_q) = \mathbf{w}_{rA}^H(\mathbf{x}; \omega_q) \mathbf{M}^A(\omega_q) \mathbf{w}_{tA}(\mathbf{x}; \omega_q). \quad (11)$$

We multiply the outputs of the two beamformers at each frequency to form the final image $I(\mathbf{x})$ as a function of each pixel $\mathbf{x}$ by implementing the energy detector

$$I_{\text{TRBF}}(\mathbf{x}) = \sum_{q=0}^{Q-1} \left|Y^A(\mathbf{x}; \omega_q) Y^B(\mathbf{x}; \omega_q)\right|^2. \quad (12)$$

The TR imager in (12) will be compared with the baseline direct subtraction beamforming imager

$$I_{\text{DSBF}}(\mathbf{x}) = \sum_{q=0}^{Q-1} \left| \frac{\mathbf{g}_B^H(\mathbf{x}; \omega_q) \mathbf{K}_t(\omega_q) \mathbf{g}_A^*(\mathbf{x}; \omega_q)}{\|\mathbf{g}_B(\mathbf{x}; \omega_q)\| \|\mathbf{g}_A(\mathbf{x}; \omega_q)\|} \right|^2, \quad (13)$$

where $\mathbf{K}_t(\omega_q)$ is the cancer tumor multipath signature matrix response at frquency ω_q. This imager (13) will perform poorly due to the uncompensated multipath.

3. FDTD SIMULATION STUDY

FDTD Breast Modeling. We simulate with the FDTD method the 2-D electromagnetic wave propagation for the purpose of

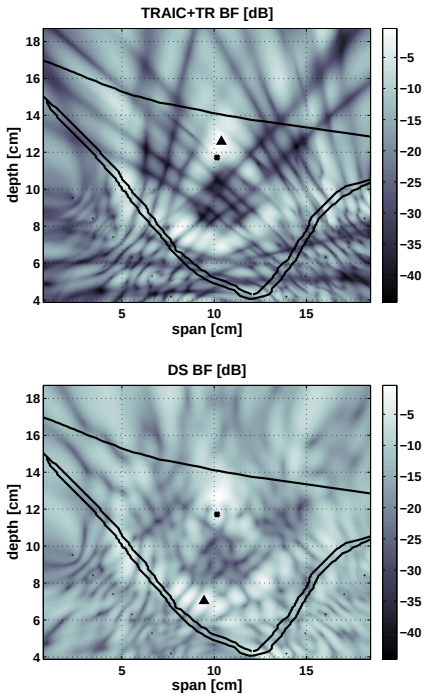

Fig. 3. Simulation imaging results. Top - TR method; Bottom - Direct subtraction method. The dot denotes the tumor location; the triangle denotes the estimated tumor location.

demonstrating the time-reversal effects. The simulation field is 20 cm by 20 cm derived from the MRI scan of a human breast shown in Fig. 1. Two linear arrays are placed at the bottom of Fig. 1 (not shown in this figure). The resulting images are shown in Fig. 3, where, for both images, the breast is in the prone position; the two layers in the lower part of the two images are the skin layers; the upper layer is the chest wall.

Breast tissue dielectric properties, including the relative permittivity ϵ_r and the conductivity σ, have been studied by several researchers [5, 6]. In this paper, we determine the permittivity value of our model based on an MRI scan of a human breast. The MRI image is an intensity image; important tissue characteristics such as blood content and blood vessels can be differentiated. We choose the logarithm of the MRI image as the permittivity values and obtain a spatial distribution of permittivity of breast tissues within the breast outline. To compare our breast model with other simulation models reported in literature, we calculate the mean value of the density, which is $\epsilon_r = 8.3$. This number is very close to the nominal permittivity value ($\epsilon_r = 9$) chosen in [5]. The variability in the breast tissues is 24% (compared to 16% in [5]), which represents the inhomogeneity of the breast tissues. The tissue conductivity is $\sigma = 0.4$ S/m; the skin is modeled as a 5 mm thick layer with $\epsilon_r = 30, \sigma = 4$ S/m; the tumor is modeled as a sphere of diameter 2 mm with $\epsilon_r = 50, \sigma = 4$ S/m. Finally, two antenna arrays, each with 7 antennas, are placed close to the skin layer in an immersion liquid with $\epsilon_r = 9, \sigma = 0$ S/m. Using immersion liquid to match the nominal permittivity value of breast tissues simplifies the computation of the beamformer weight vectors (6)-(9). However, the skin layer induces inhomogeneity in propagation due to its large permittivity value ($\epsilon_r = 30$ in our model). Fortunately, the thickness of the skin is small (5 mm) relative to the wavelength ($\lambda_c = 2.7$ cm). Thus, the overall influence of the skin on the Green's function can be approximated as a decaying factor.

The FDTD grid size is 0.5×0.5 mm^2. The resulting FDTD grid is terminated by the Perfect Matched Layer absorbing boundary condition. The probe signal is a sinc function of $10 - 12$ GHz. The time domain simulation data are converted to the frequency domain for subsequent processing.

Imaging Results. The imaging results are shown in Fig. 3. The upper figure shows the image produced by the time reversal imager; while the lower figure shows the result by the direct subtraction method. The two images are properly scaled to the same dynamic range for visual comparison purposes. The sharper and higher contrast image has more details and thus a finer resolution. For the TR image, the dynamic range is 45 dB; while for the DS image, the dynamic range is 33 dB. For both images, the dot denotes the tumor location; the triangle denotes the estimated tumor location. The TR imager shows a much better accuracy than the DS imager in locating the target, which also demonstrates the robustness of the TR imager.

4. ELECTROMAGNETIC TISSUE EXPERIMENT

Measurement Setup. We carry out the tissue differentiation experiment with pork fat and water using electromagnetic radiation. The imaging geometry is in Fig. 2. We use two C-band horn antennas, one for transmitting and the other for receiving. We collect 10 positions for each antenna as they move on a position slider. Thus, we synthesize two linear arrays shown in Fig. 2. The operating center frequency is $f_c = 5$ GHz. The channel frequency response is measured by an Agilent vector network analyzer. During the measurement, the antennas are calibrated to determine the antenna phase center at each data collection position. For each measurement, we collect a total of $Q = 201$ frequency samples in the range of $4 - 6$ GHz. The data are organized into data matrices according to (1). The collected frequency samples undergo processing to determine the cancer tumor location.

Breast Phantom. Tissue sample data suggest that malignant tumors have dielectric properties mimicking those of high-water content tissues such as muscle, whereas the surrounding normal breast tissues are more representative of low-water content fatty tissues. In our experiments, we build a simple breast phantom summarized in Table 1. We use water filled in a glass test tube of 12 cm in length and 1.5 cm in diameter to represent the cancer tumor. Pork fat that is cut into very small pieces represents the normal tissue and is placed in a plastic cup of 15 cm high and 8 cm in diameter. The relative permittivity of water is 78. It is difficult to determine

Table 1. Summary of the Breast Phantom

Human Breast	Phantom	Dimension (cm)	Permittivity
tumor	water	12×1.5 in glass test tube	78
tissue	pork fat	15×8 in plastic cup	7.5

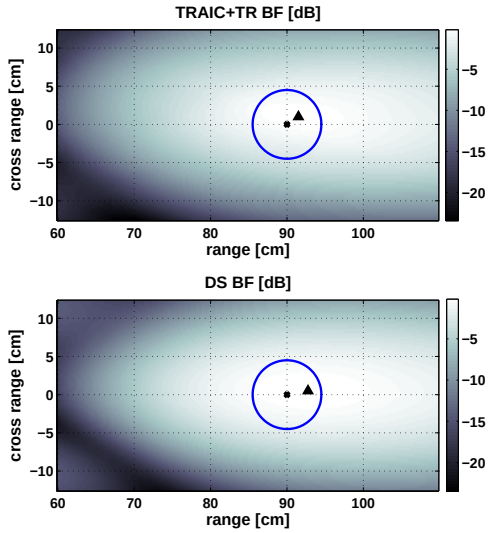

Fig. 4. Tissue imaging results. Top – TR method; Bottom – Direct subtraction method. The dot denotes the tumor location; the triangle denotes the estimated tumor location.

the dielectric constant of the fatty tissues. Here, we choose the dielectric constant 7.5 at 5 GHz given in [6] as the representative value for our experiment and for the subsequent imaging processing. During the measurement, we first measure the clutter environment that includes the fatty tissues in a plastic cup and an empty glass test tube placed in the middle of the cup. Next, we add water in the test tube and re-measure the channel response.

Imaging Results. Fig. 4 shows the imaging results using the animal tissues. During the processing, we consider only the permittivity while omitting the conductivity. Considering the fact that the transmitted electromagnetic waves travel partially in air and partially in fat, we choose the effective dielectric constant of 1.08 as an approximation when calculating the Green's function weight vectors (6)-(9). The upper figure of Fig. 4 depicts the TR image; the lower figure shows the direct subtraction image. Again, both images are properly scaled to the same dynamic range. For the TR image, the dynamic range is 23 dB; while for the DS image, the dynamic range is 21 dB. For both images, the dot denotes the tumor location; the triangle denotes the estimated tumor location. The TR imager shows better accuracy and higher resolution in locating the target.

5. CONCLUSIONS

We conducted the numerical FDTD simulation and the experimental tissue differentiation of the proposed time reversal beamforming scheme. Our imaging results demonstrate that the time reversal beamforming imager achieves better accuracy, higher robustness, and increased resolution than the conventional direct subtraction beamforming imager.

6. REFERENCES

[1] E. C. Fear, S. C. Hagness, P. M. Meaney, M. Okoniewski, and M. A. Stuchly, "Enhancing breast tumor detection with near-field imaging," *IEEE Microwave Magazine*, vol. 3, pp. 48–56, March 2002.

[2] P. M. Meaney, M. W. Fanning, T. Raynolds, C. J. Fox, Q. Fang, C. A. Kogel, S. P. Poplack, and K. D. Paulsen, "Initial clinical experience with microwave breast imaging in women with normal mammography," *Academic Radiology*, vol. 14, no. 2, pp. 207–218, March 2007.

[3] Y. Jin, Y. Jiang, and J .M. F. Moura, "Time reversal beamforming for microwave breast cancer detection," in *Proceedings of the IEEE Intational Conference on Image Processing*, San Antonio, Texas, September 2007, vol. 5, pp. 13–16, IEEE.

[4] E. C. Fear and M. A. Stuchly, "Microwave detection of breast cancer," *IEEE Transactions on Microwave Theory and Techniques*, vol. 48, no. 11, pp. 1854–1863, November 2000.

[5] A. J. Surowiec, S. S. Stuchly, J. R. Barr, and A. Swarup, "Dielectric properties of breast carcinoma and the surrounding tissues," *IEEE Transactions on Biomedical Engineering*, vol. 35, no. 4, pp. 257–263, April 1988.

[6] M. Lazebnik, L. McCartney, D. Popovic, C. B. Watkins, M. J. Lindstrom, J. Harter, S. Sewall, A. Magliocco, J. H. Booske, M. Okoniewski, and S. C. Hagness, "A large-scale study of the ultrawideband microwave dielectric properties of normal breast tissue obtained from reduction surgeries," *Physics in Medicine and Biology*, vol. 52, pp. 2637–2656, May 2007.

[7] M. Fink, G. Montaldo, and M. Tanter, "Time-reversal acoustics in biomedical engineering," *Annual Review of Biomedical Engineering*, vol. 5, pp. 465–497, August 2003.

[8] P. Kosmas and C. M. Rappaport, "Time reversal with the FDTD method for microwave breast cancer detection," *IEEE Transactions of Microwave Theory and Techniques*, vol. 53, no. 7, pp. 2317–2323, July 2005.

[9] J. M. F. Moura and Y. Jin, "Time reversal imaging by adaptive interference cancellation," *IEEE Transactions on Signal Processing*, vol. 56, no. 1, pp. 1–15, January 2008.